ACS APPLIED MATERIALS & INTERFACES

Research Article

www.acsami.org

3D Branched ZnO Nanowire Arrays Decorated with Plasmonic Au Nanoparticles for High-Performance Photoelectrochemical Water Splitting

Xing Zhang, Yang Liu,* and Zhenhui Kang*

Institute of Functional Nano & Soft Materials (FUNSOM), Jiangsu Key Laboratory for Carbon-based Functional Materials and Devices, and Collaborative Innovation Center of Suzhou Nano Science and Technology, Soochow University, Suzhou, Jiangsu 215123, China

Supporting Information

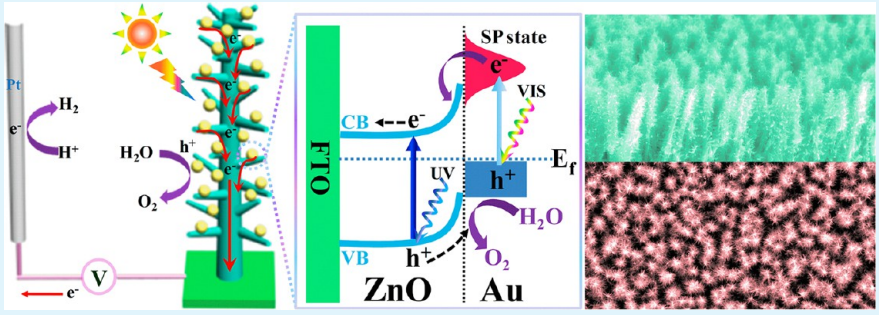

ABSTRACT: Plasmonic photoelectrochemical (PEC) water splitting is very promising in the conversion of abundant solar energy into chemical energy. However, the solar-to-hydrogen efficiencies reported so far are still too low for practical use, which can be improved by optimizing the design and synthesis of individual blocks (i. e., the compositions, sizes, shapes of the metal and the coupling semiconductors) and the assembly of these blocks into targeted three-dimensional (3D) structures. Here, we constructed a composite plasmonic metal/semiconductor photoanode by decorating gold nanoparticles (Au NPs) on 3D branched ZnO nanowire arrays (B-ZnO NWs) through a series of simple solution chemical routes. The 3D ordered Au/B-ZnO NWs photoanodes exhibited excellent PEC activities in both ultraviolet and visible region. The improved photoactivities in visible region were demonstrated to be caused by the surface-plasmon-resonance effect of Au NPs. The photoconversion efficiency of Au/B-ZnO NWs photoanode reached 0.52% under simulated sunlight illumination. This is a high value of solar-to-hydrogen efficiencies reported till nowadays for plasmonic PEC water splitting, which was mainly benefit from the extensive metal/semiconductor interfaces for efficient extraction of hot electron from Au NPs and excellent charge-carries collection efficiency of the 3D ordered Au/B-ZnO NWs photoelectrode.

KEYWORDS: *branched ZnO nanowire, gold nanoparticles, surface plasmon resonance, photoanode, water splitting*

1. INTRODUCTION

Photoelectrochemial (PEC) water splitting is a highly-efficient and eco-friendly route to meet the human demand for energy through directly converting solar energy into chemical energy for easy storage, transport and utilization in the form of hydrogen. Metal oxide semiconductors such as TiO_2, ZnO and Fe_2O_3 have been extensively explored as photoelectrode materials due to their physical and chemical stability, low cost and easy availability.[1−4] Nanometer-sized metal oxide semiconductors are particularly prevalent for water splitting applications in view of their higher surface-to-volume ratio and shorter transport path for minority carriers with respect to their bulk counterparts.[2,3] Metal oxide nanoparticles (NPs) films benefited from their huge specific surface area have been extensively studied in photovoltaic areas, however, suffered from high charge-carrier recombination loss due to the lower charge-carrier mobility resulted from the electrons trapping/scattering at grain boundaries.[5,6] Vertically oriented one dimensional (1D) arrays offer an excellent material architecture for photovoltaic applications due to their unique merits such as lower carrier recombination loss, decoupling directions of light absorption and charge-carrier collection and vectorial charge-carrier transport perpendicularly to the charge collecting substrates.[7−9] Recently, 1D nanostucture arrays of metal oxide such as TiO_2 nanowires (NWs)/nanotubes (NTs) and ZnO NWs have been extensively studied as photoelectrode materials and demonstrated to be efficient in improving the solar-to-hydrogen efficiency due to their excellent geometric construction.[10−17] However, compared with NPs, 1D NWs or NTs have smaller surface area which negatively impact the

Received: January 12, 2014
Accepted: March 5, 2014
Published: March 5, 2014

   dx.doi.org/10.1021/am500234v | ACS Appl. Mater. Interfaces 2014, 6, 4480−4489

charge-carriers capturing for water-splitting reactions.[7,18] Therefore, it's desirable to construct single-crystalline 1D nanostructure arrays of semiconductor with high surface-to-volume ratios. Fortunately, branched NWs arrays can well match the requirements as model nanostructure photoelectrode for PEC water-splitting devices. Recently, branched NWs arrays which can be either homogeneous or heterogeneous had been widely utilized for solar energy conversion due to their excellent properties such as enhanced specific surface area, high charge carries collection efficiency and easily nanoscale-integration of different functional materials.[5,19−24]

Among various metal oxide, ZnO have been extensively explored for solar energy conversion because it possesses an energy band structure and optoelectronic properties similar to those of TiO_2, while has a higher electron mobility, easier crystallization and anisotropic growth.[25,26] Electron diffusivity (D_n) in single ZnO NWs was determined to be 0.05−0.5 cm^2 s^{-1}, which is several hundred times larger than the highest reported diffusivity for TiO_2 or ZnO NPs films.[7] But, the efficiency based on ZnO NWs is still lower than ZnO or TiO_2 NPs photoanodes because of the relative lower internal surface area of ZnO NWs.[7,26] Constructing secondary NWs branches on the pristine NWs backbone have been demonstrated to be an efficient way to increase the roughness factor (defined as the total surface area per unit substrate area) and simultaneously maintain the outstanding charge-carriers collection properties as single-crystalline NWs arrays does.[19−21]Yang et al. had synthesized branched ZnO nanotetrapods with nitrogen-doping, which were then used as the photoactive materials for PEC water splitting.[19] And also, branched ZnO NWs (B-ZnO NWs) had been previously investigated as the conductive substrates for dye-sensitized solar cells.[20,21] However, limited by the large band gap, ZnO is only active in the ultraviolet (UV) region which contributes less than 5% of the total energy of solar spectrum. Many strategies have been taken to expand ZnO absorption spectrum to visible (VIS) and near-infrared region. Among these strategies, coupling with a secondary photoactive component or doping with nonmetal elements are the most prevalent, but their effectiveness are limited by the absence of long-term-stability of the secondary photoactive component or the much reduced electron-hole separation in the presence of the nonmetal species in ZnO.[10,27] For example, unmodified cadmium chalcogenide quantum dot-sensitized photoanode exhibited poor photochemical stability due to the hole-induced anodic corrosion in photoelectrochemical hydrogen generation systems.[10c] And also, nitrogen-doping in ZnO had been suggested to be deep-level defects which behaved as charge-carrier recombination centers.[27] Therefore, it's urgent to search for a strategy to simultaneously increase the light-capturing and the materials stability. Fortunately, plasmonic nanostructures of noble metal especially gold (Au) have been demonstrated to be promising for photocatalytic and energy conversion due to its tunable interactions with light in visible and infrared regions through localized surface-plasmon-resonance (SPR).[28,29] In addition, compared with semiconductor quantum dots or dyes which usually suffer from photocorrosion, Au nanostructure exhibit considerably better photostability.[30] Some pioneering work have demonstrated that Au nanostructures coupling with an optimum semiconductor can act like photosensitizers to transfer some of the absorbed plasmonic energy to an adjacent semiconductor either through resonant energy transfer or directly through hot-electron injection.[31−36] Moskovits et al. reported an autonomous photosynthetic device based on an Au nanorod arrays decorated with TiO_2 and oxygen evolution co-catalyst which obtained a ∼0.1% solar-to-hydrogen efficiency under one simulated light illumination.[32] And before too long, Wang et al. reported that they obtained a photoconversion efficiency of ∼1.1% with a plasmonic photoanode based on Au NPs modified TiO_2-based photonic crystal substrate.[34] However, so far the obtained efficiencies of their work still cannot fairly compare with using quantum dots or dyes photosensitizers in PEC devices. Typically, solar-to-hydrogen efficiency of 3.1% had been achieved on an oxide photoanode coupling with a dye-sensitized solar cell.[10b] And also, Chen et al. reported a maximum photoconversion efficiency of 1.83% of a CdTe sensitized ZnO NWs photoanode for overall water splitting.[10d] Since the thermal relaxation of hot electrons which resulted from surface plasmon decaying occurs on a femtosecond time scale (1−10 fs), even though they have a high mobile velocity (about 10^6 m s^{-1} in a typical metal), the hot electrons can still travel over distances of several nanometers before their energy is lost.[37] Therefore, the short diffusion-length limitation of the hot-electron dynamics highlights the benefit to use smaller metal nanostructures. On the other hand, the hot-electrons can survive a longer time or be transferred away for photochemical reactions through the Schottky junction at the metal/semiconductor interfaces. Consequently, an extensive metal/semiconductor interfaces would also be beneficial for the hot-electrons' extraction. It can be concluded that designing a plasmonic metal/semiconductor composite photoelectrode with smaller metal nanostructures and extensive metal/semiconductor interfaces points a bright future to maximize the solar energy harvesting and conversion efficiency.

According to the design concept proposed above, we fabricated an Au NPs modified B-ZnO NWs arrays which was later used as photoanode for PEC water-splitting. The B-ZnO NWs arrays were synthesized through a simple two-step hydrothermal process at low temperature. Subsequently, plasmonic Au NPs were decorated on the B-ZnO NWs arrays through a facile ionic layer adsorption and thermal-reduction process. The morphostructures, compositions and crystalline phases of these Au/B-ZnO NWs photoanodes were well characterized by electron microscopy, elements analyses and X-ray power diffraction analyses. Then, the PEC performances were systematically investigated and compared under simulated sunlight and visible light illumination. The results showed that the Au NPs modified B-ZnO NWs arrays photoanodes exhibited a higher PEC activity both in UV and VIS regions, compared with the Au NPs modified pristine ZnO NWs (P-ZnO NWs) photoanodes. This enhanced activity was mainly ascribed to the increased loading density (the number of Au NPs on unit substrate area) while with similar distribution density (the number of Au NPs on unit surface area of ZnO) of Au NPs and the extensive Au/ZnO interfaces which contributed the increased absorption of light and the extraction efficiency of hot electrons from Au NPs, respectively.

2. EXPERIMENTAL SECTION

2.1. Synthesis of P-ZnO NWs. Fluorine-doped tin oxide (FTO) coated glasses (1 cm ×1.5 cm) were firstly cleaned by orderly ultrasonication in acetone, ethanol and deionized water for ten minutes and then dried in N_2 stream at room temperature. The conducting surface of the FTO glass was wetted with 0.1 mL of zinc acetate ethanol solution (5 mM) and then dried naturally. Then, the FTO substrates were annealed at 320 °C for 60 min to form a dense

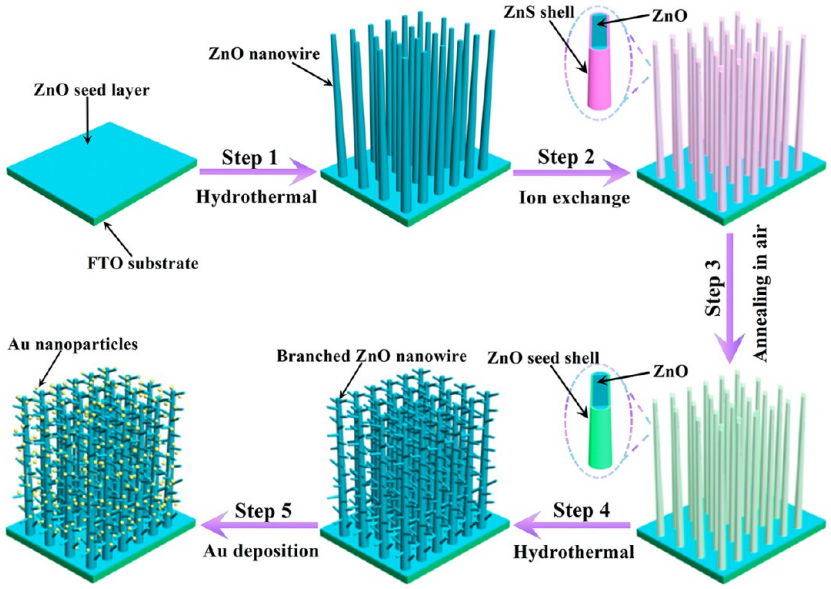

Figure 1. Schematic diagram of the main processes for the fabrication of Au NPs modified B-ZnO NWs arrays photoelectrode.

ZnO seed layer on the conducting side. Subsequently, these substrates were placed with conductive surface up into Teflon-lined stainless-steel autoclaves filled with 15 mL of zinc nitrate hydrate (25.0 mM), hexamethylenetetramine (12.5 mM), polyethylenimine (5.0 mM) and aqueous ammonia (0.5 M) aqueous solution and kept at 91 °C for 6h. After taken out from the autoclaves, these samples were repeatedly rinsed with ethanol and deionized water.

2.2. Synthesis of B-ZnO NWs. The P-ZnO NWs substrates were firstly immersed into 1 M Na_2S aqueous solution for 3 h and taken out. Then, the substrates were rinsed with deionized water for several times to remove the residual Na_2S and then dried naturally. These substrates were further annealed at 500°C for 5h in air to convert the ZnS into ZnO. Subsequently, the annealed samples were used as substrates for the second hydrothermal growth of ZnO NWs under the same experimental conditions except for being kept for 1 h at 91 °C. Finally, the samples were annealed at 500 °C for 1 h again to remove the possible organic impurities (mostly polyethylenimine) from the reaction solution used in the hydrothermal processes.

2.3. Modification of Au NPs on B-ZnO NWs. The Au NPs were in-situ deposited onto the B-ZnO NWs through a facile ionic layer adsorption and thermal-reduction approach. Firstly, the B-ZnO NWs were immersed into the $HAuCl_4$ aqueous solution (1 mM) for 30 s and then dried in N_2 stream at 70 °C. A mixing solution of 4 mL absolute ethanol and 6 mL ultrapure water was poured into a clean glass vessel and heated to boil in an electric oven which had been set to 110 °C. Subsequently, the substrate with adsorbed $AuCl_4^-$ was submerged into the ethanol/water mixing solution for 10 min. Then the trivalent Au ions were reduced to Au NPs by ethanol and a color change from white to light burgundy of the B-ZnO NWs substrates can be observed. Finally, the substrate was rinsed with deionized water and dried in N_2 stream.

2.4. Characterization of Materials. The morphologies of the samples were analyzed by using a JEOL JSM-6700F field-emission scanning electron microscope (FESEM). Transmission electron microscopy (TEM) images and element mapping were obtained by using a Tecnai G2 F20 electron microscope at an acceleration voltage of 200 kV. UV−vis absorption spectra were obtained using a Shimadzu 3600 UV−vis−NIR spectrophotometer with fine $BaSO_4$ powder as reference. The X-ray diffraction pattern of the materials was measured by a Shimadzu thin film diffractometer equipped with Cu Kα radiation (λ = 1.540598 Å). X-ray photoelectron spectroscopy (XPS) data were collected by an Axis Ultra instrument under ultrahigh vacuum ($<10^{-8}$ Torr) and by using a monochromatic Al Kα X-ray source operating at 150 W.

2.5. Electrochemical Characterization. The photoelectrode was fabricated by securing a copper wire on the exposed electric conductive parts of the FTO with a silver conducting paint. The substrate was subsequently sealed on all edges with epoxy resin except the active working areas. All electrochemical measurements were performed in a three electrode mode with a photoelectrode as the working electrode, a coiled Pt wire as counter electrode, a Ag/AgCl reference electrode, and 0.5 M Na_2SO_4 aqueous solution (with pH buffered to ~7.0) as the electrolyte. Electrochemical measurements were performed on an electrochemical analyzer (660D, CHI Instruments). The incident photon to current efficiency (IPCE) was recorded under illumination of monochromatic light from a xenon lamp using a monochromator (Jobin-Yvon, TRIAX 320) and detected by a computer-controlled Stanford SR830 lock-in amplifier with a Stanford SR540 chopper. All photoelectrodes were illuminated from the front side by a 300 W Xe lamp equipped with an AM 1.5 G filter (Model 81094, Newport) to simulate the solar spectrum. The light intensity was calibrated to 100 mW cm^{-2} by a Si diode (Model 818, Newport). Visible light illumination was obtained by passing the AM 1.5 light through a 420 nm long-wave-pass filter. The evolution of gases was measured by using a gas chromatograph with nitrogen as the carrier gas.

3. RESULTS AND DISCUSSION

Figure 1 presents the design and fabrication strategies for the plasmonic Au/B-ZnO NWs photoelectrode. The detailed synthesis procedures can be found in the Experimental Section. In brief, vertically oriented ZnO NWs firstly grew on the seeded FTO substrate through a modified hydrothermal method.[38] As far as we know, the qualities of the ZnO seed layer are strongly correlated with the natures of the synthesized ZnO NWs. Therefore, prior to the ZnO secondary-branching NWs' growth, a uniform ZnO seed shell is need to be generated on the outer-walls of the ZnO backbone NWs. Here, we first introduce a uniform ZnS layer by ion-exchanging reaction to form ZnO/ZnS core/shell NWs. The conversion of ZnO to ZnS at the surface of ZnO NWs was realized by a sulfide alkaline treatment of ZnO NWs in S^{2-} contained solution, as described in the following reaction:

$$ZnO + S^{2-} + H_2O \rightarrow ZnS + 2OH^- \quad (1)$$

This process had previously been used for creating a thin ZnS leading layer at the surface of ZnO nanorod for subsequent growth of CdS by Lu et al.[39] The ZnS shell was then converted into a ZnO nanocrystals shell by annealing at high temperature in air for adequate time.

The polycrystalline ZnO shell around the single-crystal ZnO NWs subsequently served as the seed layer for second-generation ZnO NWs' growth. It should be noted that the ZnO seed layer formed by the method reported here can be uniform and high-density regardless the slightly bending or cross-linking of the ZnO NWs. After the second hydrothermal process, B-ZnO NWs arrays which ZnO second-branching NWs grew on the ZnO backbone NWs were successfully formed. Finally, the Au NPs were decorated on the B-ZnO NWs through a facile ionic layer adsorption and reduction process.

Figure 2 are the recorded XRD patterns to exhibit the crystalline-phase evolution of the products during each

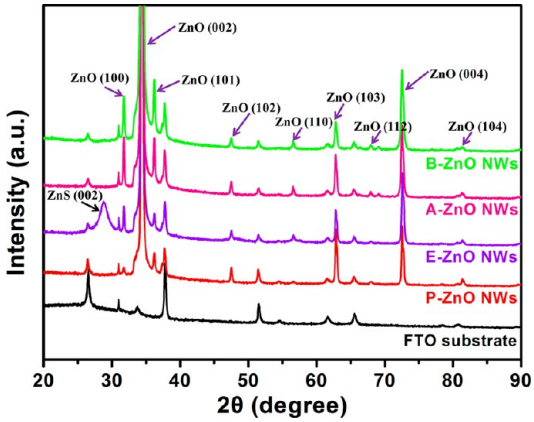

Figure 2. XRD patterns of FTO substrate, P-ZnO NWs, P-ZnO NWs etched by 1 M Na2S solution (E-ZnO NWs), E-ZnO NWs after annealing at 500 °C in air (A-ZnO NWs) and B-ZnO NWs, respectively.

procedure of the synthesis of B-ZnO NWs. By firstly subtracting the diffraction peaks of the FTO substrate, the P-ZnO NWs was identified as a wurtzite structure (JCPDS No. 79-2205) with an overwhelming diffraction peak located at 34.4° which indicating a preferred orientation of the NWs along the c-axis perpendicular to the substrate. After it has gone through an ion-exchanging etching process in Na_2S solution, a broader diffraction peaks located at 28.8° emerged in the XRD patterns of E-ZnO NWs, which can be indexed to the (002) plane of wurtzite structured ZnS (JCPDS No. 1-1280). This index was supported by energy-dispersive X-ray spectrum (EDS) of the elements analyses of the E-ZnO NWs (see Figure S1 in the Supporting Information), which demonstrated that a large amount of S element was incorporated into the ZnO NWs after the etching process. Subsequently, after suffering a thoroughly annealing process in air, the diffraction peaks of the ZnS (002) plane totally disappeared in the XRD patterns of A-ZnO NWs while the resonant diffraction peaks were similar to that of P-ZnO NWs. Simultaneously, the EDS elements analyses also shows that the S element was completely removed after the annealing process. These results persuasively certified that the ZnS could be converted to ZnO by annealing the ZnS/ZnO sample in air with temperature over 500 °C. Compared with P-ZnO NWs and A-ZnO NWs, the XRD patterns of B-ZnO NWs exhibited the same number and locations of the diffraction peaks which can also be indexed to wurtzite structured ZnO.

Electron microscopy characterizations were used to record the morphology evolutionary during the B-ZnO NWs synthesis process. Seen from the scanning electron microscopy (SEM) images as shown in Figure $3A_1$ and A_2, we can find that the P-ZnO NWs vertically grew on the FTO substrate with lengths up to 9 μm and diameters range from 50 to 200 nm. Transmission electron microscopy (TEM) and high-resolution TEM (HRTEM) images (as shown in Figure $3A_3$ and A_4, respectively) revealed that the P-ZnO NWs were single-crystalline and grew along the [0001] crystallographic orientation. After gone through the ion-exchanging etching process in Na_2S solution, there are no observable changes of the morphology of the E-ZnO NWs arrays (Figure $3B_1$) compared with that of P-ZnO NWs. The high-magnification SEM and low-magnification TEM images (as shown in Figure $3B_2$ and B_3, respectively) showed that the surface of the E-ZnO NWs became rougher than the P-ZnO NWs. Further, the HRTEM images showed that many little NPs formed on the surface of the NWs with crystal lattice spacing of 0.31 and 0.29 nm, which can be indicated to be (002) and (101) of ZnS. The results determined by the HRTEM characterization were well consistent with the results obtained from the XRD characterization. The XRD patterns of E-ZnO NWs exhibited an additional and broadening diffraction peak of ZnS (002) plane compared with that of P-ZnO NWs, which ascribed to be caused by the little ZnS NPs on the surface of ZnO NWs. These results clearly demonstrated that a polycrystalline ZnS shell formed around the ZnO NWs. There were also no observable morphology changes of the A-ZnO NWs arrays (Figure $3C_1$) except the surface of the NWs became much rougher (see Figure $3C_2$ and C_3) after the annealed process. The HRTEM image shown in Figure $3C_4$ exhibited that many NPs on the surface of the NWs with crystal lattice spacing of 0.26, 0.28, and 0.19 nm, which were ascribed to be (002), (100), and (102) of ZnO. Combined with the XRD results exhibited above, we can firmly concluded that the polycrystalline ZnS shell around the ZnO NWs core were completely converted into polycrystalline ZnO seed shell after gone through the annealing process in air. Figure $3D_1$ and D_2 are the top-view and cross-section view SEM images of the B-ZnO NWs, respectively, which show that ZnO NWs with secondary branches vertically oriented on the FTO substrate. The average lengths and diameters of the ZnO secondary branches were measured to be about 200 nm and 30 nm, respectively. The TEM and HRTEM images (as shown in Figure $3D_3$ and D_4, respectively) exhibited that the ZnO secondary branching grew on the ZnO backbone NWs with an arbitrary angular orientation and both the branches and backbones are single-crystalline NWs with preferential growth direction along the [0001]. Further, the EDS elements analyses of the B-ZnO NWs undoubtedly confirmed that only ZnO species existed (see Figure S2 in the Supporting Information). It also should be noted that increasing the second-hydrothermal-reaction time to 2 h would result in longer and cross-linked NW branches and serious fusion of NWs backbone of the B-ZnO NWs (see Figure S3 in the Supporting Information). Therefore, it's suitable to maintain the second-hydrothermal-reaction time at 1 h for obtaining a high-qualified B-ZnO NWs with high-density branches and open internal-channels in the film under the experiment conditions reported here.

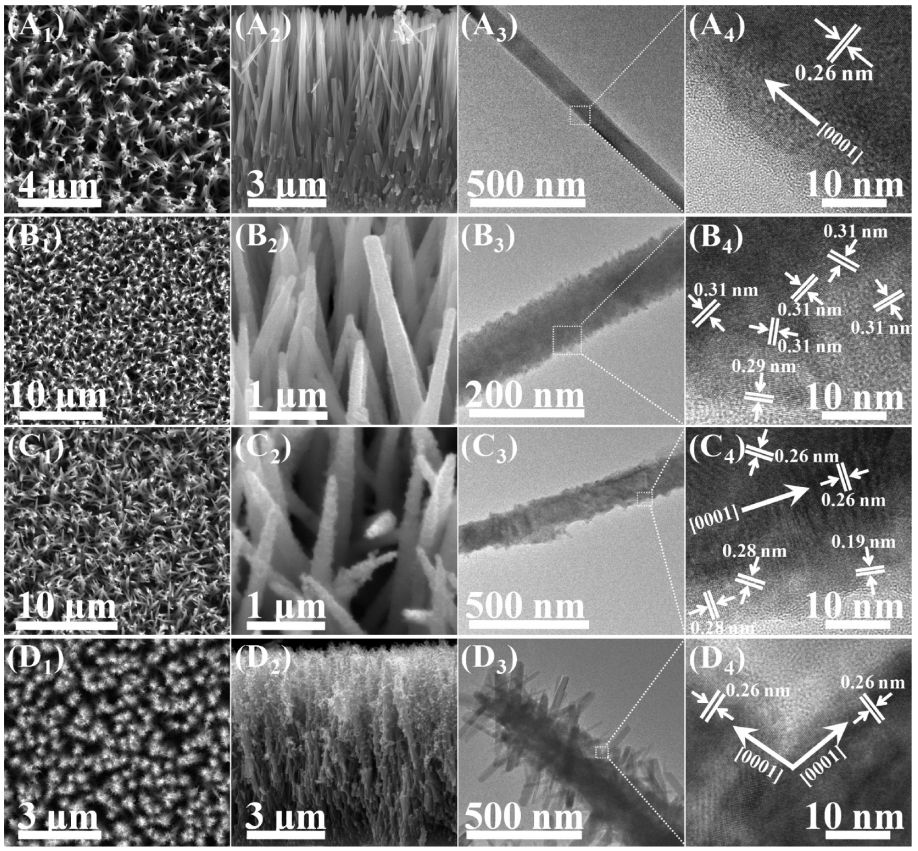

Figure 3. A_1, B_1, C_1, and D_1 are the top-view SEM images of P-ZnO NWs, E-ZnO NWs, A-ZnO NWs, and B-ZnO NWs, respectively. A_2, B_2, C_2, and D_2 are the cross-section SEM images of P-ZnO NWs, E-ZnO NWs, A-ZnO NWs, and the B-ZnO NWs, respectively. A_3, B_3, C_3, and D_3 are the low-magnification TEM images of P-ZnO NWs, E-ZnO NWs, A-ZnO NWs, and the B-ZnO NWs, respectively. A_4, B_4, C_4, and D_4 are the HRTEM images of the areas marked with white-dotted rectangular-frame in A_3, B_3, C_3, and D_3, respectively.

To examine whether Au NPs were successfully modified on the B-ZnO NWs, electron microscopy characterizations were firstly executed to give a visualized proof. Figure 4a and b showed the top-view and cross-section view SEM images of the B-ZnO NWs arrays after Au NPs modification, from which we can see that B-ZnO NWs still maintained their vertically-orientated and three-dimensional branched characteristics. The Au NPs with uniform size (in the range from 5 to 10 nm) could be found both on the backbones and branches of the B-ZnO NWs by scrutinizingly examine the high-resolution SEM images shown in the inset of Figure 4a and b. Large amount of Au NPs can be easily distinguished from the low-resolution TEM image (shown in Figure 4c) of a single Au/B-ZnO NW based on the contrast difference between ZnO and Au NPs. The average size of the Au NPs was determined to be ~8 nm by a statistical analysis of particle sizes from the TEM images. A high-resolution TEM image (shown in Figure 4d) taken from a selected area of the Au/B-ZnO NW showed that the Au NP with exposed (111) crystal face intimately loaded on the surface of the ZnO NWs branch. Further, the Au/B-ZnO NWs were investigated by scanning transmission electron microscopy (STEM) with a high-angle annular dark-field (HAADF) detector, which is sensitive to the atomic number contrast between the Au NPs and ZnO NWs. Au NPs can be easily distinguished from the STEM images (shown in Figure 4e) of a single Au/B-ZnO NW and their sizes distribution was consistent with the result obtained from the bright-field TEM characterization. The EDS element mapping of Zn, O, Au (Figure 4 g-i) from a selected area in Figure 4e illustrated that the element distribution are consistent with the structure of Au/B-ZnO. The process developed here offers a low-cost, easily-executed and in-situ method for Au NPs' modification on hierarchical and complex nanostructures. On the other hand, the XPS analyzes of the Au/B-ZnO (see Figure S5 in the Supporting Information) clearly demonstrated that metallic Au species located on the surfaces of ZnO.

The light absorption properties of the P-ZnO NWs and B-ZnO NWs before and after Au NPs modification were measured and compared over a wavelength range from 300 to 850 nm. Figure 5 shows the diffused reflectance UV−vis absorption spectra of the four films on the FTO substrates. Both the P-ZnO NWs and B-ZnO NWs exhibited a huge absorption enhancement in ultraviolet region because of the large band gap of ZnO. The optical band gap of the ZnO NWs here was estimated to be about 3.1 eV based on the converted $(ahv)^n$ versus hv curves (see Figure S6 in the Supporting Information), which is slightly lower than the previously reported band gap value of other groups.[10,25] This little deviation should be ascribed to unavoidable and insignificant carbon doping (see Figure S7 in the supporting information) during the synthesis process of the ZnO NWs which may cause red-shift of the optical absorption edge and also may resulted from a weak optical absorption of the FTO substrate.[5,19] As expected, absorption enhancements in the visible region were found both for the P-ZnO NWs and B-ZnO NWs after Au NPs modification. The characteristics of the enhanced optical absorption in the visible region were consistent with the SPR absorption of free dispersed Au NPs solution (see Figure S8 in

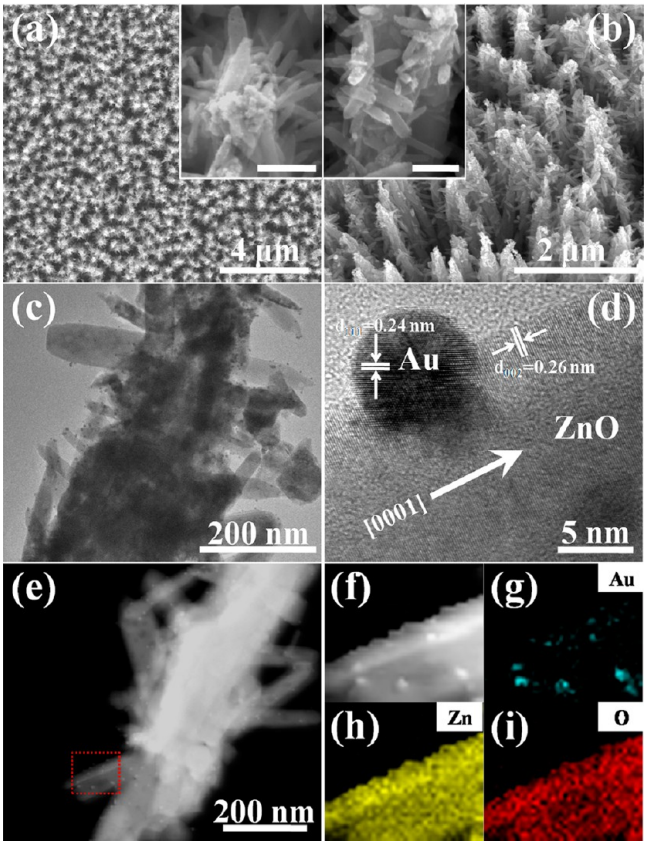

Figure 4. (a) Top-view and (b) titled 30° view SEM images of Au NPs modified B-ZnO NWs arrays. The scale bars of the inset in panels a and b are both 200 nm. (c) Low-magnification TEM images of Au NPs modified B-ZnO NWs. (d) HRTEM images taken from a selected area in panel c. (e) HAADF STEM images of Au NPs modified B-ZnO NWs. (f) Magnified STEM images from the area marked with red-dotted rectangular-frame in panel e. (g–i) Element mappings of Au, Zn, and O in the region shown in panel f.

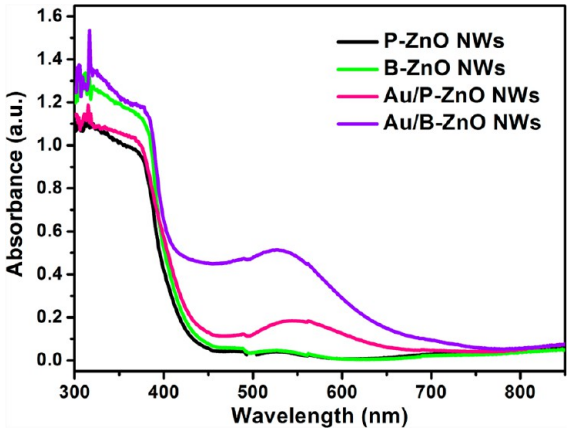

Figure 5. UV–vis absorption spectra of the P-ZnO NWs, Au NP-modified P-ZnO NWs (Au/P-ZnO NWs), B-ZnO NWs, and Au NP-modified B-ZnO NWs (Au/B-ZnO NWs).

the Supporting Information), which is an another convincing proof that the Au NPs modified on the ZnO NWs and contributed the visible light absorption. It's worth to note that the slightly red-shifted of the SPR peak of Au/ZnO composite with respect to that of freely dispersed Au NPs was due to the increased dielectric constant of the surrounding mediums. The mass percent of Au NPs determined by inductively coupled plasma atomic emission spectrometer were 7.5% for Au/B-ZnO and 7.6% for Au/P-ZnO, respectively. This result suggested that the distribution density of Au NPs on B-ZnO NWs was similar to the one on P-ZnO NWs. While the hugely increased light absorption of Au/B-ZnO in visible region revealed that the loading density of Au NPs on B-ZnO NWs was much larger than the one on P-ZnO NWs.

Electrochemical measurements were systematically performed to evaluate the PEC properties of the Au/ZnO composited photoelectrodes. A standard three-electrode electrochemical cell with a Pt wire counter electrode and an Ag/AgCl reference electrode was used for all of the PEC measurements. The electrolyte was 0.5 M Na_2SO_4 aqueous solution (with pH buffered to ~7.0) which had been bubbled with N_2 flow for 1 h to exclude the dissolved oxygen. The work electrodes were illuminated from the front side with a simulated sunlight from a 300 W Xe lamp equipped with an AM 1.5G filter. The potentials were measured versus the Ag/AgCl reference electrode and were converted to the reversible hydrogen electrode (RHE) scale using the Nernst function:[12]

$$E_{RHE} = E_{Ag/AgCl} + E^{\circ}_{Ag/AgCl} + 0.059\ pH \quad (2)$$

E_{RHE} is the converted potential versus RHE. $E_{Ag/AgCl}$ is the external potential measured against the Ag/AgCl reference electrode. $E^{\circ}_{Ag/AgCl}$ is the standard electrode potential of Ag/AgCl reference electrode (0.1976 V versus RHE at 25 °C). Figure 6a shows a set of linear sweep voltammetry of P-ZnO NWs, B-ZnO NWs, Au/P-ZnO NWs, and Au/B-ZnO NWs photoelectrodes under dark and simulated sunlight illumination. The dark scans from −0.1 to 1.4 V vs RHE only exhibited a small background current density at μA cm^{-2} scale. While the current densities of all photoelectrodes promptly increased after the external potential exceeded the onset potential around 0.3 V vs. RHE under simulated sunlight illumination. It's noted that both the Au NPs modified P-ZnO NWs and B-ZnO NWs photoelectrodes exhibited larger photocurrent densities in the whole potential widow than the corresponding ZnO NWs photoelectrodes without Au NPs modification. This result suggested a positive role of Au NPs in enhancing the photoactivity of ZnO NWs photoelectrodes. As can be seen from Figure 6b, the chronoamperomertic I–t curves recorded under chopped light illumination at 1 V vs RHE revealed an instantaneous photoelectric response of all the photoelectrodes. In addition, the Au/B-ZnO NWs yielded a photocurrent density reached 1.45 mA cm^{-2}. Further, the photoconversion efficiencies for PEC water splitting of these photoanodes were estimated by following equation:[40]

$$\eta = I(1.23 - V_{app})/P_{light} \quad (3)$$

V_{app} is the applied external potential versus RHE. I is the externally measured current density at V_{app}. P_{light} is the power density of the incident light. As shown in Figure 6c, the maximum photoconversion efficiency of Au/B-ZnO NWs photoelectrodes was 0.52%, which was double the one of B-ZnO NWs (0.24%) and 1.7 times larger than the Au/P-ZnO NWs (0.30%). The above electrochemical results convincingly concluded that both the Au NPs modification and the 3D branches structure of the ZnO NWs played positive roles in enhancing the PEC activity of ZnO.

It's essential to quantify the amount of the evolution gases in PEC water splitting experiment. Figure 6d displays the

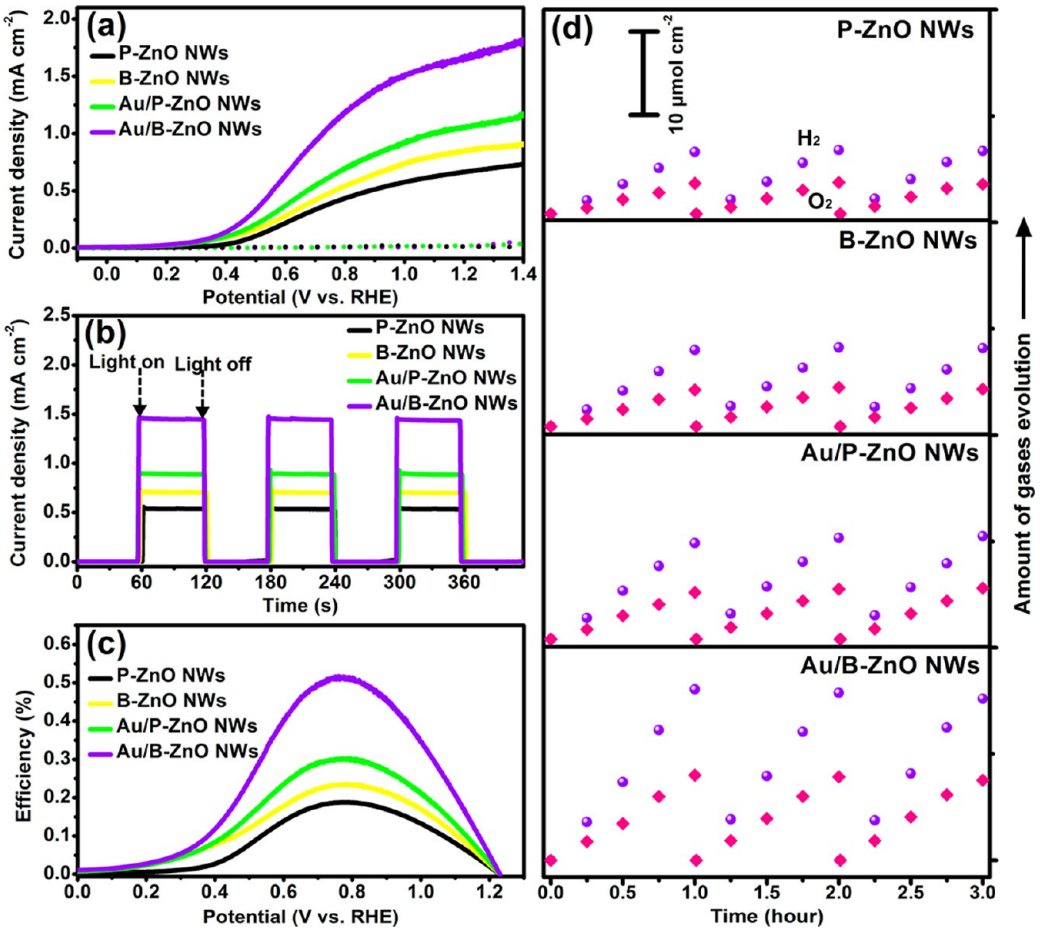

Figure 6. Photoelectrochemical behaviors of P-ZnO NWs, B-ZnO NWs, Au/P-ZnO NWs, and Au/B-ZnO NWs photoanodes under simulated sunlight illumination (a) Linear sweep voltammetry (20 mV/s) of these photoanodes in darkness (dotted lines) and under illumination (solid lines). (b) Chronoamperometric $I-t$ curves under chopped illumination at 1 V vs RHE. (c) Calculated photoconversion efficiency as a function of applied voltage vs RHE. (d) Time courses of gases evolution for these photoanodes with imposed external potentials derived from the extreme point of corresponding photoconversion efficiency.

evolution of H_2 and O_2 gases versus time for the four kinds of photoelectrodes operated under simulated sunlight illumination. For all the photoelectrodes, H_2 and O_2 with a stoichiometric ratio of approximately 2:1 simultaneously evolved from the surface of Pt counter electrode and photoelectrode, respectively. Also, the linear increase of the amount of H_2 and O_2 revealed an excellent stability of these photoelectrodes under operation condition. The H_2 evolution amount of these four photoelectrodes were in the order of P-ZnO NWs (average 7.4 μmol h^{-1} cm^{-2}) < B-ZnO NWs (average 9.2 μmol h^{-1} cm^{-2}) < Au/P-ZnO NWs (average 11.6 μmol h^{-1} cm^{-2}) < Au/B-ZnO NWs (average 19.6 μmol h^{-1} cm^{-2}). All the photoelectrodes exhibited a Faradic efficiency around 95%, which were determined by comparing the quantities of gases produced and the amount of charge that passed through the circuit, suggesting high photochemical activity and stability of these photoelectrodes. The slight deviation from a 100% Faradic efficiency may be caused by some unavoidable gas leakage or dissolution in the electrolyte solution.

Incident-photon-to-current-conversion efficiency (IPCE) tests were utilized to investigate the specific PEC active spectra of the P-ZnO NWs, B-ZnO NWs, Au/P-ZnO NWs, and Au/B-ZnO NWs photoanodes. For better distinguishing the differences, the IPCE spectra were divided into two parts which located in UV and VIS region (as shown in Figure 7a and 7b), respectively. Seen from Figure 7a, one can found that the B-ZnO NWs exhibited a noticeable improvement of the IPCE values with respect to the P-ZnO NWs in the interband-transition absorption region of ZnO. This improvement of PEC activity of the B-ZnO NWs can be ascribed to the enhanced light capturing ability and the increased semiconductor/liquid interfaces which was benefit for charge transport and chemical reaction. The excellence of branched 1D array for PEC water splitting had also been demonstrated by other research groups, previously.[5,22] And also, both the P-ZnO NWs and B-ZnO NWs obtained an slightly improved IPCE values in UV region with Au NPs modification. This increased UV PEC activity may result from an effective surface passivation and electric-field amplification effect of Au NPs as recently demonstrated by Pu et al.[35] In the VIS region, both the P-ZnO NWs and B-ZnO NWs exhibited observable PEC activity for the reason that the photon's energy in the visible region is lower than the band gap energy of ZnO. However, there are huge improvements of PEC activity of both the P-ZnO NWs and B-ZnO NWs in the VIS region after the modification of Au NPs. The IPCE spectra in the VIS region feature like the SPR absorption spectrum of Au NPs, which better illustrated that the enhanced PEC activity in the visible region is caused by the SPR effect of the modified Au NPs. As the photon flux in VIS region is much larger than in

dx.doi.org/10.1021/am500234v | ACS Appl. Mater. Interfaces 2014, 6, 4480−4489

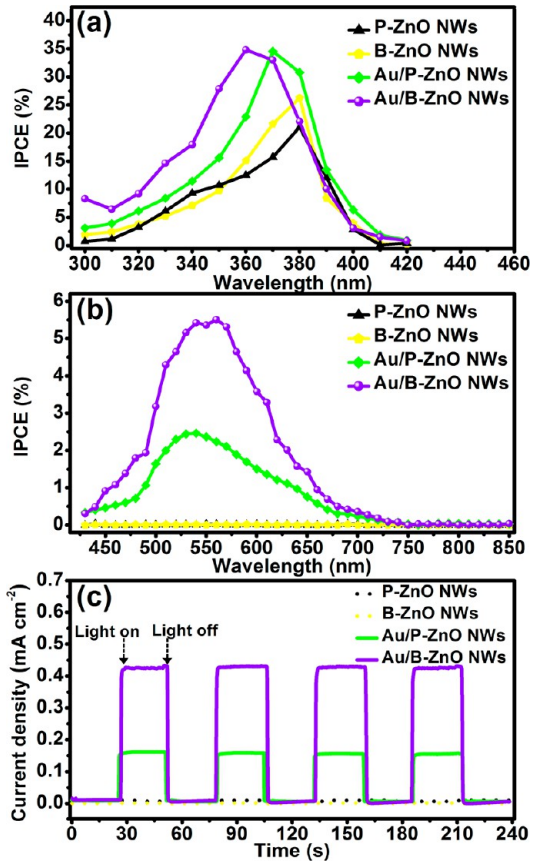

Figure 7. (a, b) IPCE spectra of the P-ZnO NWs, B-ZnO NWs, Au/P-ZnO NWs, and Au/B-ZnO NWs photoanodes collected at 1 23 V vs RHE in wavelength window of 300−420 and 420−850 nm, respectively. (c) Chronoamperomertic *I*−*t* curves collected at 1 V vs RHE with repeated on/off cycles of simulated sunlight coupled with a 420 nm long-wave-pass filter.

UV region according to the solar spectrum, the remarkably increased PEC activity in visible region was the main reason for the obtained higher photoconversion efficiency under simulated sunlight illumination. Further, we performed chronoamperomertic *I*−*t* test with chopped light illumination to investigate the photoelectric response behavior of the four photoelectrodes in VIS region. The results shown in Figure 7c exhibited a sharp increase of current density of the Au/ZnO composite photoanodes when exposed in the VIS light. And also, the photocurrent density of the Au/ZnO NWs reached ∼0.42 mA cm^{-2} under VIS light illumination, which is comparable to the one obtained by ZnO NWs photoanodes in the UV region.

On the basis of the extensive comparisons of the PEC properties among the four kinds of photoelectrodes, the main mechanisms were proposed to explain the huge enhanced PEC water splitting efficiency of the Au/B-ZnO NWs photoelectrode. As illustrated in the left panel of Figure 8, the excellent electron collection efficiency of the Au/B-ZnO NWs photoelectrode, benefiting from the high electron mobility of single-crystalline ZnO NWs and the vertical electron collection of the array structure, played vital role in improving the PEC properties by reducing the recombination of electrons and holes. And also, the 3D branch structure of the Au/B-ZnO NWs efficiently increased the roughness factor and Au NPs loading density which were both favorable to increase the light-capturing ability. Three main mechanisms had been proposed

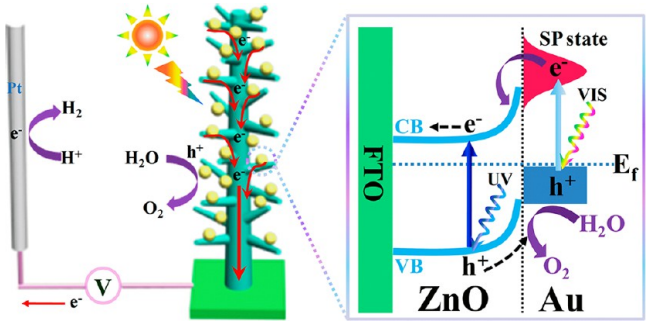

Figure 8. Main mechanisms for explaining the enhanced PEC water slitting efficiency of the Au/B-ZnO NWs photoelectrode. Left panel: Simplified schematic diagram of the PEC water splitting cell composed of the Au/B-ZnO NWs photoanode. Right panel: Energy level diagram for the SPR-mediated electron transfer (ET) from photo-excited Au NPs to the neighboring ZnO in VIS region and direct electron-hole excitation in ZnO in UV region.

to explain the effects of plasmonic metal nanostructures on PEC properties of plasmonic metal/semiconductor photoelectrode:[28,29] (1) SPR-mediated hot electrons transfer (ET) from metal to semiconductor, 2) resonant photons scattering and 3) localized electromagnetic field (LEMF) enhancement. The resonant photon scattering mechanism could be firstly excluded for the Au/ZnO composited photoelectrode reported here since it normally occurs in large plasmonic nanostructures (larger than ∼50 nm in diameter).[28] The LEMF mechanism improves the PEC activity mainly by selectively increasing the rate of interband transitions in the semiconductor due to the interaction of the localized electric field with the neighboring semiconductor.[41,42] Here, the Au NPs supported SPR at the wavelength in VIS region, where the photon energy are inefficient to lead to the formation of electron/hole pairs in ZnO in the radiated energy transfer process. So, the LEMF mechanism could also be ruled out as the main reason for the huge enhanced PEC activity of the Au/ZnO composite photoelectrode. In this case, the SPR-mediated ET process was believed to be the main contributor to the improved PEC activity of the Au/ZnO composite photoelectrode under VIS light illumination. As illustrated in the right panel of Figure 8, surface plasmons in Au NPs are photoexcited by visible light illumination and decay to hot electron-hole pairs on a femtosecond time scale, with the hot electrons transiently occupying the surface plasmon states (SP states) above the Fermi level (E_f). Subsequently, a significant fraction of the hot electrons were injected into the conduction band of ZnO either by overcoming the Schottky barriers at the Au/ZnO interface or through a tunneling effect. Then, the left energetic holes in Au NPs are filled by electrons from reduction species.[28,32,33] Here, the energetic holes in the Au NPs were mainly exhausted by water oxidation, which had been demonstrated by many other research groups.[32−36,43] The non-equilibrium electrons in the conduction band of ZnO were then transferred to the counter electrode to execute water reduction with a moderate assistance of an external potential.

Although high for a plasmonic metal/semiconductor photoelectrode system, the reported solar-to-hydrogen efficiency (0.52%) of the Au/B-ZnO NWs is still unsatisfactory for practical use. But, the facile fabrication strategies of the Au/B-ZnO NWs photoelectrode endow them powerful competiveness for large-scale practical applications. Fortunately, there are still many rooms for further improving the efficiency by

optimizing this 3D metal/semiconductor photoelectrode system. Straightforward optimizing the size, shape, or loading density of the plasmonic Au NPs may further enhance the IPCE and the photoresponse range in visible region or even in infrared region. And also, optimizing the matching of the plasmonic metals and semiconductors may also enhance the intrinsic PEC performances of the semiconductor by SPR-induced electromagnetic field effect.

4. CONCLUSIONS

We designed and fabricated a plasmonic metal/semiconductor composite photoelectrode by modifying Au NPs on B-ZnO NWs arrays through a series of facile solution chemical routes. The Au/B-ZnO NWs photoanodes exhibited a hugely enhanced PEC activity under simulated sunlight illumination, which yielded a solar-to-hydrogen efficiency of 0.52%. These improved PEC performances were ascribed to be three main positive effects of the Au/B-ZnO NWs, as systematically compared with the P-ZnO NWs, B-ZnO NWs and Au/P-ZnO NWs. First, the SPR-mediated ET process from excited Au NPs to ZnO largely extended the PEC activity of Au/ZnO composite photoelectrode in visible region. Second, the 3D branch structure of the B-ZnO NWs offered a hugely enhanced roughness factor which was beneficial for increasing the loading amount of Au NP (while with the similar distribution density as Au/P-ZnO) and thus maximizing the light-capturing efficiency. Simultaneously, the extensive Au/ZnO interfaces and little sizes of the Au NPs were very essential for high-efficient extraction of hot electron from Au NPs. Third, the branches and the backbones of the B-ZnO NWs were both single-crystalline which were beneficial for charge carries transport due the high electron mobility. And also, the huge increased semiconductor/liquid interfaces effectively contributed to photochemical reaction rate and hence reduced the recombination loss of electron-hole pairs. This work reported here offers a good example for designing of plasmonic metal/semiconductor composited photoelectrode by optimized the synergistic effects between them.

■ ASSOCIATED CONTENT

Supporting Information

EDS analyses of E-ZnO, A-ZnO, and B-ZnO, SEM images of B-ZnO with extending second-growth time, SEM and TEM images of Au/P-ZnO, XPS analyses of Au/B-ZnO, UV−vis absorption spectra of P-ZnO, E-ZnO, A-ZnO, and B-ZnO, UV−vis absorption spectra of Au NPs aqueous solution, and UV−vis transmittance spectrum of the 420 nm long-wave-pass optical filter. This information is available free of charge via the Internet at http://pubs.acs.org/.

■ AUTHOR INFORMATION

Corresponding Authors

*E-mail: yangl@suda.edu.cn. Fax: +86-512-65882846. Tel:+86-512-65880956.

*E-mail: zhkang@suda.edu.cn. Tel:+86-512-65880957.

Notes

The authors declare no competing financial interest.

■ ACKNOWLEDGMENTS

This work is supported by the National Basic Research program (973 Program) (2012CB825803, 2013CB932702), the National Natural Foundation of China (51132006, 21073127, 21071104), the specialized Research Fund for the Doctoral Program of Higher Education (20123201110018), a Suzhou Planning Project of Science and Technology (ZXG2012028), a Foundation for the author of National Excellent Doctoral Dissertation of China (200929), and a Project funded by the Priority Academic Program development of Jiangsu Higher Education Institutions.

■ REFERENCES

(1) Walter, M. G.; Warren, E. L.; McKone, J. R.; Boettcher, S. W.; Mi, Q.; Santori, E. A.; Lewis, N. S. Solar water splitting cells. *Chem. Rev.* **2010**, *110*, 6446−6473.

(2) Osterloh, F. E. Inorganic nanostructure for photoelectrochemical and photocatalytic water splitting. *Chem. Soc. Rev.* **2013**, *42*, 2294−2320.

(3) Chen, H. M.; Chen, C. K.; Liu, R.-S.; Zhang, L.; Zhang, J.; Wilkinson, D. P. Nano-architecture and material designs for water splitting photoelectrodes. *Chem. Soc. Rev.* **2012**, *41*, 5654−5671.

(4) Kronawitter, C. X.; Vayssieres, L.; Shen, S.; Guo, L.; Wheeler, D. A.; Zhang, J. Z.; Antoun, B. R.; Mao, S. S. A perspective on solar-driven water splitting with all-oxide hetero-nanostructures. *Energy Environ. Sci.* **2011**, *4*, 3889−3899.

(5) Cho, I. S.; Chen, Z.; Forman, A. J.; Kim, D. R.; Rao, P. M.; Jaramillo, T. F.; Zheng, X. Branched TiO_2 nanorods for photoelectrochemical hydrogen production. *Nano Lett.* **2011**, *11*, 4978−4984.

(6) Feng, X.; Zhu, K.; Frank, A. J.; Grimes, C. A.; Mallouk, T. E. Rapid charge transport in dye-sensitized solar cells made from vertically aligned single-crystal rutile TiO_2 nanowires. *Angew. Chem., Int. Ed.* **2012**, *124*, 2781−2784.

(7) Law, M.; Greene, L. E.; Johnson, J. C.; Saykally, R.; Yang, P. Nanowire dye-sensitized solar cells. *Nat. Mater.* **2005**, *4*, 455−459.

(8) Tang, J.; Huo, Z.; Brittman, S.; Gao, H.; Yang, P. Solution-processed core−shell nanowires for efficient photovoltaic cells. *Nat. Nanotechnol.* **2011**, *6*, 568−572.

(9) Fan, Z.; Razavi, H.; Do, J.; Moriwaki, A.; Ergen, O.; Chueh, Y.-L.; Leu, P. W.; Ho, J. C.; Takahashi, T.; Reichertz, L. A.; Neale, S.; Yu, K.; Wu, M.; Ager, J. W.; Javey, A. Three-dimensional nanopillar-array photovoltaics on low-cost and flexible substrates. *Nat. Mater.* **2009**, *8*, 648−653.

(10) (a) Yang, X.; Wolcott, A.; Wang, G.; Sobo, A.; Fitzmorris, R. C.; Qian, F.; Zhang, J. Z.; Li, Y. Nitrogen-doped ZnO nanowire arrays for photoelectrochemical water splitting. *Nano Lett.* **2009**, *9*, 2331−2336. (b) Brillet, J.; Yum, J.-H.; Cornuz, M.; Hisatomi, T.; Solarska, R.; Augustynski, J.; Graetzel, M.; Sivula, K. Highly efficient water splitting by a dual-absorber tandem cell. *Nat. Photonics* **2012**, *6*, 824−828. (c) Seol, M.; Jang, J.-W.; Cho, S.; Lee, J. S.; Yong, K. Highly efficient and stable cadmium chalcogenide quantum dot/ZnO nanowires for photoelectrochemical hydrogen generation. *Chem. Mater.* **2013**, *25*, 184−189. (d) Chen, H. M.; Chen, C. K.; Chang, Y.-C.; Tsai, C.-W.; Liu, R.-S.; Hu, S.-F.; Chang, W.-S.; Chen, K.-H. Quantum dot monolayer sensitized ZnO nanowire-array photoelectrodes: True efficiency for water splitting. *Angew. Chem., Int. Ed.* **2010**, *122*, 6102−6105.

(11) Hoang, S.; Berglund, S. P.; Hahn, N. T.; Bard, A. J.; Mullins, C. B. Enhancing visible light photo-oxidation of water with TiO_2 nanowire arrays via cotreatment with H_2 and NH_3: Synergistic effects between Ti^{3+} and N. *J. Am. Chem. Soc.* **2012**, *134*, 3659−3662.

(12) Hoang, S.; Guo, S.; Hahn, N. T.; Bard, A. J.; Mullins, C. B. Visible light driven photoelectrochemical water oxidation on nitrogen-modified TiO_2 nanowires. *Nano Lett.* **2012**, *12*, 26−32.

(13) Park, J. H.; Kim, S.; Bard, A. J. Novel carbon-doped TiO_2 nanotube arrays with high aspect ratios for efficient solar water splitting. *Nano Lett.* **2006**, *6*, 24−28.

(14) Miao, J.; Yang, H. B.; Khoo, S. Y.; Liu, B. Electrochemical fabrication of ZnO−CdSe core−shell nanorod arrays for efficient photoelectrochemical water splitting. *Nanoscale* **2013**, *5*, 11118−11124.

(15) Zhang, X.; Wang, F.; Huang, H.; Li, H.; Han, X.; Liu, Y.; Kang, Z. Carbon quantum dot sensitized TiO_2 nanotube arrays for photoelectrochemical hydrogen generation under visible light. *Nanoscale* **2013**, *5*, 2274−2278.
(16) Zhang, X.; Huang, H.; Liu, J.; Liu, Y.; Kang, Z. Carbon quantum dots serving as spectral converters through broadband upconversion of near-infrared photons for photoelectrochemical hydrogen generation. *J. Mater. Chem. A* **2013**, *1*, 11529−11533.
(17) Shankar, K.; Basham, J. I.; Allam, N. K.; Varghese, O. K.; Mor, G. K.; Feng, X.; Paulose, M.; Seabold, J. A.; Choi, K.-S.; Grimes, C. A. Recent advances in the use of TiO_2 nanotube and nanowire arrays for oxidative photoelectrochemistry. *J. Phys. Chem. C* **2009**, *113*, 6327−6359.
(18) Ye, M.; Xin, X.; Lin, C.; Lin, Z. High efficiency dye-sensitized solar cells based on hierarchically structured nanotubes. *Nano Lett.* **2011**, *11*, 3214−3220.
(19) Qiu, Y.; Yan, K.; Deng, H.; Yang, S. Secondary branching and nitrogen doping of ZnO nanotetrapods: Building a highly active network for photoelectrochemical water splitting. *Nano Lett.* **2012**, *12*, 407−413.
(20) Cheng, H.-M.; Chiu, W.-H.; Lee, C.-H.; Tsai, S.-Y.; Hsieh, W.-F. Formation of branched ZnO nanowires from solvothermal method and dye-sensitized solar cells applications. *J. Phys. Chem. C* **2008**, *112*, 16359−16364.
(21) Dai, H.; Zhou, Y.; Liu, Q.; Li, Z.; Bao, C.; Yu, T.; Zhou, Z. Controllable growth of dendritic ZnO nanowire arrays on a stainless steel mesh towards the fabrication of large area, flexible dye-sensitized solar cells. *Nanoscale* **2012**, *4*, 5454−5460.
(22) Kargar, A.; Sun, K.; Jing, Y.; Choi, C.; Jeong, H.; Zhou, Y.; Madsen, K.; Naughton, P.; Jin, S.; Jung, G. Y.; Wang, D. Tailoring *n*-ZnO/*p*-Si branched nanowire heterostructures for selective photoelectrochemical water oxidation or reduction. *Nano Lett.* **2013**, *13*, 3017−3022.
(23) Hwang, Y. J.; Wu, C. H.; Hahn, C.; Jeong, H. E.; Yang, P. Si/InGaN core/shell hierarchical nanowire arrays and their photoelectrochemical properties. *Nano Lett.* **2012**, *12*, 1678−1682.
(24) Liu, C.; Tang, J.; Chen, H. M.; Liu, B.; Yang, P. A fully integrated nanosystem of semiconductor nanowires for direct solar water splitting. *Nano Lett.* **2013**, *13*, 2989−2992.
(25) Zhang, Q.; Dandeneau, C. S.; Zhou, X.; Cao, G. ZnO nanostructures for dye-sensitized solar cells. *Adv. Mater.* **2009**, *21*, 4087−4108.
(26) Chen, W.; Qiu, Y.; Yang, S. Branched ZnO nanostructures as building blocks of photoelectrodes for efficient solar energy conversion. *Phys. Chem. Chem. Phys.* **2012**, *14*, 10872−10881.
(27) (a) Wang, G.; Yang, X.; Qian, F.; Zhang, J. Z.; Li, Y. Double-sided CdS and CdSe quantum dot co-sensitized ZnO nanowire arrays for photoelectrochemical hydrogen generation. *Nano Lett.* **2010**, *10*, 1088−1092. (b) Gu, Q. L.; Ling, C. C.; Brauer, G.; Anwand, W.; Skorupa, W.; Hsu, Y. F.; Djurisic, A. B.; Zhu, C. Y.; Fung, S.; Lu, L. W. Deep level defects in a nitrogen-implanted ZnO homogeneous *p*−*n* junction. *Appl. Phys. Lett.* **2008**, *92*, No. 222109. (c) Tarun, M. C.; Iqbal, M. Z.; McCluskey, M. D. Nitrogen is a deep acceptor in ZnO. *AIP Adv.* **2011**, *1*, No. 022105.
(28) Linic, S.; Christopher, P.; Ingram, D. B. Plasmonic-metal nanostructures for efficient conversion of solar to chemical energy. *Nat. Mater.* **2011**, *10*, 911−921.
(29) Hou, W.; Cronin, S. B. A review of surface plasmon resonance-enhanced photocatalysis. *Adv. Funct. Mater.* **2013**, *23*, 1612−1619.
(30) Warren, S. C.; Thimsen, E. Plasmonic solar water splitting. *Energy Environ. Sci.* **2012**, *5*, 5133−5146.
(31) Tian, Y.; Tatsuma, T. Mechanisms and applications of plasmon-induced charge separation at TiO_2 films loaded with gold nanoparticles. *J. Am. Chem. Soc.* **2005**, *127*, 7632−7637.
(32) Mubeen, S.; Lee, J.; Singh, N.; Kramer, S.; Stucky, G. D.; Moskovits, M. An autonomous photosynthetic device in which all charge carriers derive from surface plasmons. *Nat. Nanotechol.* **2013**, *8*, 247−251.
(33) Lee, J.; Mubeen, S.; Ji, X.; Stucky, G. D.; Moskovits, M. Plasmonic photoanodes for solar water splitting with visible light. *Nano Lett.* **2012**, *12*, 5014−5019.
(34) Zhang, Z.; Zhang, L.; Hedhili, M. N.; Zhang, H.; Wang, P. Plasmonic gold nanocrystals coupled with photonic crystal seamlessly on TiO_2 nanotube photoelectrodes for efficient visible light photoelectrochemical water splitting. *Nano Lett.* **2013**, *13*, 14−20.
(35) Pu, Y.-C.; Wang, G.; Chang, K.-D.; Ling, Y.; Lin, Y.-K.; Fitzmorris, B. C.; Liu, C.-M.; Lu, X.; Tong, Y.; Zhang, J. Z.; Hsu, Y.-J.; Li, Y. Au nanostructure-decorated TiO_2 nanowires exhibiting photoactivity across entire UV−visible region for photoelectrochemical water splitting. *Nano Lett.* **2013**, *13*, 3817−3823.
(36) Chen, H. M.; Chen, C. K.; Chen, C.-J.; Cheng, L.-C.; Wu, P. C.; Cheng, B. H.; Ho, Y. Z.; Tseng, M. L.; Hsu, Y.-Y.; Chan, T.-S.; Lee, J.-F.; Liu, R.-S.; Tsai, D. P. Plasmon inducing effects for enhanced photoelectrochemical water splitting: X-ray absorption approach to electronic structures. *ACS Nano* **2012**, *6*, 7362−7372.
(37) Chalabi, H.; Brongersma, M. L. Plasmonics: Harvest season for hot electrons. *Nat. Nanotechol.* **2013**, *8*, 229−230.
(38) Xu, C.; Shin, P.; Cao, L.; Gao, D. Preferential growth of long ZnO nanowire array and its application in dye-sensitized solar cells. *J. Phys. Chem. C* **2010**, *114*, 125−129.
(39) Lu, Z.; Xu, J.; Xie, X.; Wang, H.; Wang, C.; Kwok, S.-Y.; Wong, T.; Kwong, H. L.; Bello, I.; Lee, C.-S.; Lee, S.-T.; Zhang, W. CdS/CdSe double-sensitized ZnO nanocable arrays synthesized by chemical solution method and their photovoltaic applications. *J. Phys. Chem. C* **2012**, *116*, 2656−2661.
(40) Murphy, A. B.; Barnes, P. R. F.; Randeniya, L. K.; Plumb, I. C.; Grey, I. E.; Horne, M. D.; Glasscock, J. A. Efficiency of solar water splitting using semiconductor electrodes. *Int. J. Hydrogen Energy* **2006**, *31*, 1999−2017.
(41) Ingram, D. B.; Linic, S. Water splitting on composite plasmonic-metal/semiconductor photoelectrodes: Evidence for selective plasmon-induced formation of charge carriers near the semiconductor surface. *J. Am. Chem. Soc.* **2011**, *133*, 5202−5205.
(42) Seh, Z. W.; Liu, S.; Low, M.; Zhang, S.-Y.; Liu, Z.; Mlayah, A.; Han, M.-Y. Janus Au-TiO_2 photocatalysts with strong localization of plasmonic near-fields for efficient visible-light hydrogen generation. *Adv. Mater.* **2012**, *24*, 2310−2314.
(43) Thiyagarajan, P.; Ahn, H.-J.; Lee, J.-S.; Yoon, J.-C.; Jang, J.-H. Hierarchical metal/semiconductor nanostructure for efficient water splitting. *Small* **2013**, *9*, 2341−2347.